Improved Prediction of Losses with Large Eddy Simulation in a Low-Pressure Turbine

Kenji Miki[1*], Ali Ameri[1,2]

[1]NASA Glenn Research Center, Cleveland, OH (*kenji.miki@nasa.gov)

[2]The Ohio State University, Columbus, OH

ABSTRACT

There is a need to improve predictions of losses resulting from large eddy simulations (LES) of low-pressure turbines (LPT) in gas turbines. This may be done by assessing the accuracy of predictions against validation data and understanding the source of any inaccuracies. LES is a promising approach for capturing the laminar/turbulent transition process in a LPT. In previous studies, the authors utilized LES to model the flow field over a Variable Speed Power Turbine (VSPT) blade and successfully captured characteristic features of separation/reattachment and transition on the suction side at both the cruise (positive incidence) and take-off conditions (negative incidence) and as well, simulated the effect of free-stream turbulence (FST) on those phenomena. The predicted pressure loading profiles agreed well with the experimental data for both a high and a low FST case at a Reynolds number of Re_{ex}=220,000. In this paper, we present wake profiles resulting from computations for a range of FST values. Although the predicted wake profiles for the lowest FST case (Tu=0.5%) matched the experimental data, at higher FST (Tu=10-15%,) the wake was wider than the experimentally measured wake and for both cases were displaced laterally when compared to the experimental measurements. In our investigation of the causes of the said discrepancies we have identified important effects which could strongly influence the predicted wake profile. Predicted losses were improved by assuring the validity of the flow solution. This was done by utilizing spectral analysis to scrutinize the dynamic behavior of the wake and determine solution accuracy resulting from low mesh density and low accuracy of convective modeling.

INTRODUCTION

Enhancement to the performance of low-pressure turbines (LPTs) and thereby realizing further reductions in fuel burn in gas turbine engines may be achieved by assessing new designs by accurate accounting of losses. Small variations in the flow path can result in significant changes in aerodynamic losses. This is particularly true with the back stages of the LPTs where the local Reynolds number can be quite low. Accurate flow modeling is needed to allow the determination of flow losses.

Most computer programs used to perform Large Eddy Simulations (LES), utilize a second-order finite volume method. In this paper, we will discuss the accuracy of predicted losses using such frameworks. LES computations are inherently more accurate than the more common and inexpensive Reynolds-Averaged Navier-Stokes (RANS) computations. As stated by Marconcini *et al*. [1], some of the weaknesses in the ability of RANS to predict losses compared to LES include both the level of losses as well as the "maturity" of losses, where LES computations achieve mixed-out status in a much smaller distance. Also, more is expected from LES computations in terms of the accuracy of predictions of such phenomena as laminar/turbulent transition and flow separation at low to moderate turbulence intensity and the resulting losses. In order to achieve resolution of large eddies and hence a high accuracy, grid suitability needs to be established by ascertaining the -5/3 dependence of the computed energy spectra in the inertial range [2]. In addition, a range of low x^+, y^+, and z^+, which are the dimensionless wall grid resolution based on the wall shear stress in the domain, can provide good accuracy of the results [3].

It is possible that the grid size and count still play an important role even after the above criteria is met. For example, requiring a higher resolution inside the boundary layers can better simulate the boundary layer itself and its exchange of turbulence with the free stream. Using Direct Numerical Simulation (DNS) type accuracy and grid resolution Przytarski and Wheeler [4] showed that further enhancing the grid resolution does result in large differences in the losses. In fact, they learned that an increase in grid resolution in their computation of a compressor blade changed a transition mechanism on the suction side from separation to attached flow transition and surprisingly increased the loss by 7%. The refinement was by a factor of four. Pichler et al. [5] studied the requirements and made recommendations for the proper resolution of scales of turbulence in DNS for a LPT simulation at a Reynolds number =60,000 and Tu=3.5%.

Recently Lee *et al.* [6] have discussed the effect of "calculation parameters," such as span of the computational domain (in quasi-three-dimensional LES computations) and the location of the exit boundary as well as the time step used on the computed loss predictions. They show minor effects on the computed losses due to the last two effects when confronted with inaccuracies in their off-design predictions. Due to the large angle of attack in their computations, they found significant variation in the computed losses due to the extent of the span of the computational domain. Medic *et al.* [7] computed losses for a set of Pack blades using a quasi-3d LES

framework. They were able to compute the losses with good accuracy for a case with a moderate free-stream turbulence. Their computations with a low free-stream turbulence yielded higher levels of error 12-16% at low Reynolds number of 30,000 ostensibly due to numerical errors. For a highly loaded transonic blade with separated flow, Harnieh *et al.* [8] were able to achieve an accuracy of approximately 85% for the losses with their quasi-3d LES computations.

In a previous work [2], we conducted a series of LES simulations to investigate the flow field over VSPT blade at both the cruise (positive incidence) and take-off conditions (negative incidence) [9] and investigated the effect of free-stream turbulence (FST) on the separation [2]. As a part of validation and verification (V&V) of the computations, in that work, a set of checks of the component of the computational model were performed as summarized below:

- The then newly implemented turbulence model (LES-LDKM) was tested against the isotropic turbulence, and the calculated energy decay rate was verified to agree with the reference value [10].
- The grid resolution of the base mesh (85 million points) in the vicinity of the walls was investigated by the instantaneous distribution of local y_1^+, It was confirmed that the calculated averaged grid spacing, y_1^+ was ~2 at the wall. x^+ and z^+ values were ~ 8 and 24.
- The grid resolution inside the flow field was examined by calculating the Pope criterion, $\mathcal{M}$ [11]. It was found that $\mathcal{M}$ was mostly below ~0.1 in the freestream region, indicating that our base mesh was likely fine enough to resolve FST based on that test.
- To check whether the synthetic turbulence imposed at the inlet became physical before it reached the blade, we calculated the power spectral density of the normalized axial velocity component at different axial locations and confirmed that the spectral slope followed the Kolmogorov -5/3 law. This constituted an additional validation for the LES subgrid model and the numerical scheme.
- Introducing synthetic turbulence can generate spurious pressure waves, which could contaminate the numerical solutions [12]. To confirm that our solutions were not subject to such waves, we checked the time-histories of the density field by probing the flow at two different xial locations, one at the inlet ($X/C_x = -1$) and one at the outlet ($X/C_x = 2,$ between wakes) and found there were not any spurious pressure waves [2].
- The pressure coefficient distribution along the blade surface at the midspan for the low-FST case and the high-FST case were calculated and compared with the experimental data. Good agreement was achieved for both cases.

In this paper, we use the above validated numerical approach to predict the wake profile and the total pressure loss. This is a challenging task, as the wake is quite sensitive to the separation/reattachment/transition at low FST and transition at high FST on the blade. We utilized spectral analysis of the flow solutions to ensure a valid and accurate final result.

EXPERIMENTAL SETUP

The experimental data of the VSPT cascade was acquired at the NASA Transonic Turbine Blade Cascade Facility (CW-22) [13-15]. The uniqueness of the facility is the cascade's large scale and continuous run capability at engine relevant conditions (The tested *Re* exit number range: 212,000 to 2,120,000. The tested inlet flow angle range, β *:* -16.8^o to 50.0^o, and inlet *Ma* from 0.192 to 0.435). An overview and the key dimensions of the experimental configuration are shown in Fig. 1 (a) and Table 1. The turbulence grid, which is designed to generate isotopic turbulence in the freestream region, is installed upstream of the blade row. The inlet turbulence intensity (*Tu*) without a turbulence grid was documented to range from 0.25% to 0.40% [15] and, with the grid, *Tu* can go up to 15%. The inlet conditions were measured at Station 0 located at $L_{s,0}/C_x$= -0.415 axial-chords upstream of the cascade, and the wake losses are measured at $L_{s,1}/C_x$ = 1.07 axial-chords downstream of the trailing edge of the blade row. The detailed descriptions of this experimental facility can be found in references [13-15].

Experimental Uncertainties

The experimental uncertainties associated with the wake profile C_{pt} for the low FST and the high FST are ±0.0422 and ±0.0443, respectively. It is worth mentioning that the variation in the wake profiles among blades is non-negligible due to the fact that the turbulence intensity varies pitchwise (and less spanwise) along the measurement Station (i.e., each blade experiences a slightly different Tu. The spanwise and pitchwise variation of the normalized Tu is ΔTu =±4.1% and ΔTu =±15% at the Station 0). Therefore, all calculated wakes are shown with three profiles from blade 4, 5 and 6, which are located in the middle of the experimental domain. More detailed explanation as to how to evaluate the uncertainties is provided in [16]. The experimental uncertainties associated with the pressure coefficient are ±0.046(about the size of symbols of data point). In addition, the inaccuracies incurred in the positioning of the probe for characterizing the wake though are important, such errors in this facility are reported to be insignificant.

COMPUTATIONAL METHOD

The computer code Glenn-HT [17] was used in this work. Glenn-HT solves the unsteady compressible Navier-Stokes equations. Glenn-HT has been continuously updated over the past two decades at the NASA Glenn Research Center (GRC). Glenn-HT is designed for structured multi-block grids using a massively parallel algorithm. In this study, a dual time-stepping procedure is adopted in which the solution implicitly advances in physical time and the explicit four-stage Runge-Kutta scheme is called in pseudo-time. The transport equations are spatially discretized using a cell-centered finite volume method. The AUSM^{+}-up scheme [18] is used to calculate the inviscid flux, thus minimizing the numerical dissipation. Throughout this study, the minmod function and the piecewise-linear function are used as the limiters of the MUSCL scheme to achieve 2nd order or 3rd order accuracy [19] in space while the time-advancing is of second order.

In this paper, the localized dynamic *k*-equation model (LDKM) with the Favre filter proposed by Kim and Menon [20] is used for all test cases. The key idea of LDKM is that the model coefficients appearing in the Reynold stress and the subgrid dissipation are dynamically evaluated based on the assumption [21] that “similarity" exists in the nature of isotropic turbulence between the largest unresolved scales and the smallest resolved scales. It has been reported that the LDKM is capable of capturing the small-to-large scale energy cascade as well as transition. In addition, there is no *ad-hoc* model parameter, which needs to be tuned for different applications. The detailed explanation of LDKM may be found in [20].

Computational Grid

There are three grids used in this study. In our previous studies [2, 9], we generated a grid of nearly 85 million points (base mesh) that covers the full span of the passage and axially from one chord upstream to one chord downstream. There was no symmetry assumption at the midspan as made by other researchers such as by Cui *et al.* [22], who used approximately 30 million points to resolve the half passage with one endwall. In addition to the base mesh, we generated two other meshes, a coarse one, with 10 million points, and a fine one with 170 million points. All grids were generated with the GridPro™ software.

TEST AND BOUNDARY CONDITIONS

The flow conditions used in the present simulations are summarized in Table 2 and Fig.1 (b). The inlet boundary condition is specified based on the experimental conditions [13-15]. Total pressure, temperature and the inlet angle are specified. Although the values

of *Tu* and *Ts* are reported in [15], there are some uncertainties associated with these values when they are imposed at the inlet boundary since the turbulence generating grid is not in the current computational setup and the turbulence grid was normal to the inlet flow but not to the blade leading edge plane. Therefore, the measured values of these quantities are treated as nominal values. A model generating a realistic inlet turbulence is required to provide time dependent turbulent flows, which are characterized by the specified mean flow profile, *Tu* and *Ts* and thus the Reynolds stress profiles. Here we use the digital filtering approach of Klein *et al.* [23] due to its simplicity of implementation and economy of computational resources. Although the inlet turbulence generated by this type of method follows prescribed second order statistics, it is still required that we add a buffer zone in the upstream region so that there is enough time for a synthetic turbulent flow to develop realistic turbulent structures (e.g., higher moments) before it reaches the cascade.

A constant pressure boundary condition for the exit and a no-slip boundary condition is used for the walls. Periodicity is assumed in the blade-to-blade direction. Symmetry was not used in the spanwise direction as described earlier.

NUMERICAL RESULTS

In this subsection, some numerical results of VSPT calculations are presented. For the simulation cases, 960 or 1440 processors (depending on the mesh sizes) of Xeon Gold 6148 sockets (2.4 GHz and 192 GB of memory) of the Pleiades supercomputer located at the NASA Advanced Supercomputing facility were used.

Characteristic of Incoming Turbulence

The transport of freestream turbulence into the boundary is a key factor for understanding the unsteady boundary layer behavior. Thus, characterizing the simulated incoming turbulence is critical in this study. We have calculated *Tu*s at two different axial locations, X/C_x=-1 (inlet) and X/C_x=-0.5 (close to the measurement point), and the results are summarized in Table 3. Considering the spanwise and pitchwise variations reported in [15], the calculated *Tu* is reasonably close to the upper limit of the experimental data when the inlet *Tu* is set to be 15%. To meet the lower limit of the experimental data (~8.4 %), we reduced the inlet *Tu* to 10%. To confirm the isotropic nature of the inflow turbulence, u'_{rms}/U_0, v'_{rms}/U_0, w'_{rms}/U_0, as well as cross-components ($u'v'$, $u'w'$, and $v'w'$) are calculated in the freestream of H-FST1 at X/C_x=-0.5. Although there is some variation among u'_{rms}/U_0,

v'_{rms}/U_0, and w'_{rms}/U_0, we can reasonably confirm isotropicity of the incoming turbulence in this setup. Wanting to perform a sensitivity analysis, we performed all the calculations with the same turbulent inflow conditions, including the parameters used in the digital filtering approach. A different degree of numerical dissipation using different grid resolutions and numerical schemes should result in different turbulence characteristics near the blade, which is a part of the effect to be studied in this study.

Wake Predictions

Two cases were considered; one at a low free-stream turbulence (Tu=0.5%), henceforth designated as "L-FST", and one at a high-FST case (Tu=15%) ("H-FST1"). For the L-FST case, the plot of time-averaged friction on the blade surface in previous work [2] indicated separation on the suction side. The H-FST1 case, the flow on the suction side was not separated due to early transition.

Figures 2 (a) and (b) present the predicted total pressure loss coefficient, C_{ptot}, which is defined by $C_{ptot}=(P_{t,in}-P_T)/(P_{t,in}-P_{ex})$ defined for the experimental data. The profiles are compared in the wake at X/C_x=1.07. The wake is thinned for the H-FST1 case compared to the L-FST case. This is consistent with the state of the boundary layer described in the last paragraph.

To assess the accuracy of the predictions compared with the experimental data, we introduced three metrics: 1) the horizontal shift at the peak, ΔX, 2) the discrepancy in the maximum pressure loss coefficient, ΔC_{pt}, and 3) the difference between the Full Width at Half Maximum (FWHM) values of the experimental and the predicted values, $\Delta W = |\Delta W_{exp} - \Delta W_{LES}|$.

For both cases, the mesh resolution was 85 million points, and the AUSM$^+$-up with the 2nd order scheme was used. For the low-FST case, although the predicted profile is slightly shifted from the data, there is excellent agreement in the shapes which is evidenced by a match between the shifted profile (gray) by ΔX=0.05**pitch* and the data. (We confirmed that the predicted total pressure loss coefficients for the low-FST case using the implicit LES model [8] and the present results using the LES-LDKM model are very similar.) Other criteria, $\Delta C_{pt}/C_{pt\text{-}exp}$=4.2% and $\Delta W/\Delta W_{exp}$ =0.38 appear to be well within the experimental uncertainty.

For the high-FST case, however, there is a noticeable discrepancy between the prediction and the data in the sense that all three metrics significantly worsen compared to the Low-FST case. For instance, ΔX=0.1**pitch* is twice as large as the one for the low-FST case, and the wake profile is much wider than the experimental wake, which can be seen by a large disagreement between the shifted profile (gray) and the data. The ensuing sections attempt to find the source of the discrepancy and the remedy.

Analysis of the Wake Profile at H-FST1

It was observed that the wake profile stays stable and narrow for most of the flow-through time, but occasionally becomes unstable, resulting in a very thick wake. We refer to this type of event as a "hiccup" herein. The instantaneous density gradient profiles of the stable and unstable wakes are shown in Figs. 3 (a) and (b). When the wake is stable, the recirculation bubble does not exist and the undulated edge of the thick boundary layer, which is related to the Kelvin-Helmholtz (K-H) instabilities, is not seen. As reported [2], the effect of increasing *Tu* seems to be suppressing the separation bubble by energizing the boundary layer due to mixing with the freestream turbulence. When a hiccup takes place, the thick boundary layer and the resulting large wake appear. This resembles the case at a lower level of *Tu*. The transition mechanism from the stable wake to the unstable wake is not clear.

After a series of checks as described earlier, this poor prediction of the wake profile for the high-FST case (and the unexpected hiccups) obliged us to perform further analysis in order to identify the root-cause of this issue. This study should help us establish a best practices approach to accurately predict the wake loss, which is of primary interest in terms of component efficiency of the turbine. To determine the cause of transition from a stable wake to an unstable wake, we adopt a systematic approach as illustrated in the fishbone diagram (see Fig. 4). We categorize the issues into four groups as follows:

1. The first issue group is "user" caused, which is not related to physics, but to how we calculate the system. For instance, it could be possible that the calculation is not performed long enough to collect the relevant statistics. In fact, Lee *et al*., [5] reported that for some off-design computations, the statistics (such as the profile loss) may not converge even with the common practice of averaging periods of a few flow through times.
2. The second issue group is "numerics". For instance, the grid resolution and the high/low-order schemes should be in this category. One of the hypotheses for the cause of the hiccup is that our scheme is not dissipative enough. Alternatively, it might be necessary to use a further refined mesh (or a high-order scheme), although we confirmed that the value of y_1^+ in the vicinity of the wall and the Pope criterion inside the flow field are comparable to the recommended values given the base mesh (85 million points). Also, the spurious pressure waves reflected at the inlet and exit boundaries would be in this category. Please note that our calculations were not contaminated by any spurious pressure waves in the upstream and downstream regions [2].

3. The third group of issues relates to the "input", which includes the boundary condition (e.g., *Tu, Ts*, etc.). Simon *et al*., [24] reported that the reattachment location is sensitive to the intensity and length scales of FST. Also, our previous study demonstrated that the size of the separation bubble varied with *Tu* and the integral length scale, *Ts,* at the inlet [2].
4. The final group of issues relates to the "physics". An example of a physical mechanism would be some documented flow instability that would also be present in the experiment, but not detected due to the slow response time of the pneumatic pressure probes. It is however desirable to have a tool to help identify other physics that may be causing the unstable wake.

To proceed with the rest of the analysis, we introduced a probe that we carefully located at the edge of the wake in order to obtain the time-history of the total pressure, $P_T/P_{T,0}$. The probe location (white circle) is shown in Fig. 5(c). The time-history of $P_T/P_{T,0}$ for the H-FST1 case is shown in Fig. 5(a). It is observed that when the wake is stable, $P_T/P_{T,0}$ is around 0.95. However, when a hiccup occurs, $P_T/P_{T,0}$ suddenly drops below 0.9. To quantify the stability of the wake, we take the statistic of the time-history and calculate the normalized time intervals of three scenarios: $P_T/P_{T,0} > 0.95$ (the wake is very stable), $P_T/P_{T,0} > 0.925$ (a hiccup does not occur) and $P_T/P_{T,0} < 0.9$ (a hiccup occurs). We show those statistics in Fig. 5(b). For the H-FST1 case, the wake is stable (i.e., no hiccup) for ~88% of the computational time. However, the wake becomes very unstable for ~1% of the time, indicating unexplained instability in the system. This affects the unsteady solution but not the average solution which indicated no separation. Nonetheless, the resolution of this could lead to the resolution of the issue besetting the total pressure loss profile deviation from the experiment as shown in Fig. 2(b).

Convergence and Large Numerical Dissipation (H-FST2)

Next, we would like to check the convergence of the statistics and the effect of the numerical dissipation using a coarser mesh (10 million points) with *Tu*=15% (called "H-FST 2"). We opted to perform this test, instead, on the coarser grid recognizing that the same test on our fine grid requires time and resources beyond those which we can afford. To this end, we collected and calculated the required statistics for every 15 ms. Please note that the flow-through time ($\sim C_x/U_o$) based on the inlet *Ma* number is ~2 ms. The resulting normalized time interval of seven segments is shown in Fig. 6. For the four first time segments, we observe some variability in the statistics which tends to stabilize with time. After a long calculation time (more than 100 flow-through times), we confirm that the occurrence of the hiccups is not a temporary phenomenon that occurs only in the initial stage of the calculations. This test rules out the possibility of insufficient running time to obtain stationary results.

The predicted total pressure loss coefficient, the time-history of $P_T/P_{T,0}$ of one selected segment and the normalized time interval for the case H-FST2 are shown in Figs. 7 (a)-(c). Compared with the time-history of the total pressure and the statistic of the H-FST1 case (See Figs. 5 (a) and (b)), the wake is noticeably more unstable namely, ~0.1 of the time is when $P_T/P_{T,0} < 0.9$. This is a counterintuitive result. Using a coarser mesh should increase the numerical dissipation and smooth out the small-scaled flow features, which suppress transient phenomena. However, using the coarse mesh made the wake significantly more unstable, and the resulting wake profile much wider. Compared with the wake of the H-FST1 case (See Fig. 2 (b)), all three metrics ($\Delta X=0.12*pitch$, $\Delta C_{pt}/C_{pt\_exp}$=30%, and $\Delta W/\Delta W_{exp}$ =103%) deteriorated. We speculated that with this coarse mesh some important mechanics that would suppress the hiccups continue to be underresolved.

Incoming Turbulence Intensity (H-FST3)

Next, the effect of the inflow turbulence (*Tu*) on the stability of the wake was investigated. For this purpose, we continued to use the coarse mesh (10 million points) and lowered the *Tu* value down to 10 % and compared the wake behavior to the 15% case. The resulting time-history of $P_T/P_{T,0}$, the normalized time interval, and the predicted total pressure loss coefficient are shown in Figs. 8 (a)-(c). It is observed that the wake is more unstable than the previous two cases (H-FST1 and H-FST2), and ~0.18 of the computational time is when $P_T/P_{T,0} < 0.9$. Although the resulting wake is slightly thinner than the one of the H-FST2 case, the peak is overestimated by $\Delta C_{pt}/C_{pt\text{-}exp}$ =35%. We also tested the higher *Tu* (not shown here) and found that higher *Tu* does not improve the wake stability. From these observations, it was surmised that the effect of suppressing the unstable boundary layer (and the recirculation bubble) by mixing with the freestream turbulence is not accurately evaluated in this coarse mesh simulation. In order to justify this hypothesis, we decided to test the high-order scheme and to examine the dynamic behavior of the wake given the coarse mesh. Using this type of higher order scheme does not appreciably add to the computational cost but is akin to running a finer mesh.

High-Order Scheme (H-FST4)

In this subsection, we used third-order MUSCL scheme developed by Cada and Torrilhon [19] coupled with the AUSM$^+$-up scheme. The predicted wake profile as well as the time-history of $P_T/P_{T,0}$, and the normalized time interval statistic are shown in Figs. 9 (a)-(c). In this case (called "H-FST4"), all numerical setting and the boundary conditions including *Tu* and the mesh remain the same as the H-FST3 case. It was found that the wake becomes noticeably more stable than the H-FST3 case. Only in ~0.07 of the computational

time $P_T/P_{T,0}$ is < 0.9. As a consequence, all three metrics improved (ΔX=0.11**pitch*, $\Delta C_{pt}/C_{pt\_exp}$=23%, and $\Delta W/\Delta W_{exp}$=74.8%). This encouraging result confirms that suppressing the instability of the wake is related to the numerics and how accurately the model evaluates the effect of mixing with the freestream turbulenc

However, one of the remaining questions is what kind of physics triggers the persisting dynamic behavior of the wake. In other words, which aerodynamics phenomena are under- or over-estimated by the current numerical setup although we have followed the conventional procedures of LES and successfully captured some characteristic features of separation/transition on the suction side at both the cruise (positive incidence) and take-off conditions (negative incidence) [2,9] To address this question, we perform the detailed spectral analysis in the next subsection.

Spectral Analysis (H-FST1, H-FST2, H-FST4)

In a previous study [2], we demonstrated the use of spectral analysis in determining the location of separation and the dynamic behavior of a separation bubble. Figure 10 shows one of the key results of the L-FST case from our previous study. The time-averaged shear stress profile on the suction side (see Fig. 10 (a)) clearly indicates the location of the separation bubble starting at X/C_x=0.65 and the transition to turbulence taking place at X/C_x=0.75. In addition, we recorded the time-histories of the axial velocity component at three locations, X/C_x=0.6 (red), X/C_x=0.7 (blue) and X/C_x=0.8 (green) and used FFT to calculate the discrete Fourier transform of these time histories. The resulting FFTs (see Fig. 10 (c)) show that there is a strong oscillation at X/C_x=0.7 (blue), which is consistent with the observation from Fig. 10 (a). More importantly, the peak frequency (~700 [Hz]) is very close to the measurements obtained in the similar experimental setup of Volino [25]; an encouraging evidence that the spectral analysis is indeed capable of capturing dynamic behavior.

Here, we would like to extend the capability of the spectral analysis so that we can identify correlation between dynamic behaviors at two locations, one of which is the wake in this study. The procedure is outlined as follows:

a. collect the time histories of the axial velocity component at the various locations and the total pressure at the wake (see the top figures of Fig.11)
b. use FFT to calculate the discrete Fourier transform of each profile (see the bottom figures of Fig.11)
c. calculate a correlation coefficient, *r*, between the two FFTs.

Figure 12 shows the example of two sets of the time-histories of the axial velocity component from the H-FST4 case: (a) at the pressure side (X/Cx=0.5) and (b) at the suction side (X/C_X=0.75) against the total pressure at the wake. The FFTs of these profiles are shown at

the bottom. Looking at Fig. 12 (a), two profiles are highly correlated (r=0.71), and the peaks of FFTs coincide well. For the weakly correlated case with r=0.33 (see Fig. 12 (b)), the peaks of FFTS do not coincide, indicating that these two dynamics behave differently. A cut-off frequency of 3000 [Hz] was used.

Figure 13 shows the correlation coefficients of the selected test cases (H-FST1, H-FST2, and H-FST4). (Please note that the H-FST1 case predicts the most stable wake among the three cases, and the predicted wake profile is closest to the data.) There are several key features that may be observed in the table:

- For using the coarse mesh (H-FST2 and H-FST4), the large area on the suction side shows strong correlation with the wake, which may indicate the existence of a persisting unstable boundary layer and/or a separation bubble. Also, the edge of the bubble is shifted upstream with reduction of FST or reduction of the order of accuracy. This trend is similar to what we observed for the low-FST cases in the sense that a large separation bubble appears, and the separation is shifted upstream [2].
- For the H-FST1 case, we still observe a small area (between X/C_x=0.65 and X/C_x =0.75), which shows high correlation with the wake or separation bubble activity. Such undesirable separation and reattachment should not exist for a high free-stream turbulence condition which may indicate that this numerical setup still does not accurately capture the interaction between the free-stream turbulence and the boundary layer.
- For the H-FST1 case and the H-FST4 case, there is a strong correlation between the incoming turbulence and the wake. However, the H-FST2 case shows a much weaker correlation between the two events. Using the coarse mesh with the 2nd order scheme seems to smooth out the freestream turbulence due to excessive numerical dissipation.
- For the H-FST1 case, there is a strong correlation between the flow dynamics on the pressure side and the wake, which originates at the leading edge and which seems to synchronize with the incoming turbulence. In fact, the free-stream turbulence buffets the boundary layer on the pressure side, which correlates to the dynamics of the wake. The two coarser grid cases exhibit this behavior to a lesser extent but more for the 3rd order case that the second.

Figure 13 suggests that when we use the coarse mesh or the low-order scheme, the dynamics of the wake is strongly correlated with the separation bubble or the unstable boundary layer. However, for the case using the fine mesh or the high-order scheme, the correlation to the suction side boundary layer is diminished suggesting that the effect of the separation on the dynamics of the wake has become weaker. Instead, the incoming turbulence and the flow dynamics of the pressure side become more important.

These observations are illustrated in Fig.14. There are three effects; the free-stream turbulence (for a given *Tu* input), suction-side dynamics, (e.g., boundary layer instability and separation bubble,) and the pressure side dynamics, which may be contributing to the stability of the wake. The color of an arrow indicates the nature of the relationship between two entries, destabilizing (red), stabilizing (blue), and interacting (green).

Stable Wake Prediction (H-FST5, H-FST7)

The wake stability analysis suggests that a higher-order scheme or a finer mesh (or both) could improve our wake loss prediction. To test this hypothesis, we went back to the original setup (H-FST1: 85 million mesh and *Tu*=15%) and changed the 2nd order scheme to the 3rd order scheme. The predicted total pressure loss coefficient and the time-history of the total pressure at the wake are shown in Figs. 15 (a) and (b). It is confirmed that a hiccup indeed does not occur anymore (i.e., the computational time when $P_T/P_{T,0} < 0.9$ is zero) and $P_T/P_{T,0}$ remains ~0.95 at all time. Switching to the high-order scheme stabilizes the wake. Although there is some improvement in the prediction of C_{pt} compared with the one of the H-FST1 case, three metrics ($\Delta X=0.08*pitch$, $\Delta C_{pt}/C_{pt\_exp}$ =14%, and $\Delta W/\Delta W_{exp}$ =53.6%) still need to be improved.

Next, we run the case using a finer mesh (170 million points with a refinement of ~1.26 in each direction) and the 3rd order scheme (H-FST7). The predicted wake loss coefficient is shown in Fig. 16. We observe that overall agreement with the experimental data is significantly improved. For instance, the difference of the peak C_{pt} from the experimental data is only $\Delta C_{pt}/C_{pt\_exp}$ =6%, and $\Delta W/\Delta W_{exp}$ reduces to 4.4 % well within the measurement accuracy of the three measured wakes. The profile, if shifted by $\Delta X*pitch=0.06$ (gray), matches the data well.

Although the shift still exits, the prediction accuracy evaluated by three metrics for the high-FST case is comparable to the low-FST case. From these results, we conclude that the determination of the mesh quality for performing LES simulations of the wake predictions should be done with additional care.

Grid Dependency Study (H-FST4, H-FST6, H-FST7)

For the sake of completeness, we would like to compare the numerical predictions using three different meshes (10 million mesh (H-FST4), 85 million mesh (H-FST6), and 170 million mesh (H-FST7)) under the same operating condition (*Tu*=10 %). Figure 17

depicts the time-averaged total pressure profiles at the midspan (Z/C_x=0.4225) and at the wake (X/C_x=1.07). For the coarse mesh, there is a large total pressure loss appearing in the upstream region on the suction side, and a large separation zone follows downstream. The large loss core seen in the wake is related to the separation as well as the ensuing transition. Using the fine mesh, separation was significantly suppressed and the size and the magnitude of the loss in the loss core decreased. The base mesh case, naturally, falls between the two cases in (a) and (c). The resulting pressure coefficients along the blade surface at the midspan and the total pressure loss coefficients of the three cases are shown in Fig. 18 (a) and (b). The predicted pressure coefficients agree with the experimental data very well except near the trailing edge where the profile of H-FST4 deviates from the experimental data. The predicted wake profiles are asymptotically approaching the experimental data as the mesh density increases. It is also observed that the left edges of all three profiles coincide, and the shift is ~0.05**pitch*. Thus, the shift appears to be invariant with the numerical accuracy.

In the preceding paragraphs, based on our analysis, we claimed that the grid resolution was the cause of the hiccup that we observed and eliminated by using better resolution or a higher order scheme. In the following sections we will describe the effect of grid resolution a.) on the predicted free-stream turbulence and its interaction with the boundary layer, b.) on the boundary layer profiles, and c.) on the turbulent kinetic energy (TKE) content of the boundary layer.

a. Free Stream Turbulence

The instantaneous vorticity magnitude, which represents turbulence activity, at the midspan, is shown in Fig. 19. When using the coarse mesh (a), more laminarization occurs due to flow acceleration by the favorable pressure gradient and numerical dissipation through the passage. This is evidenced by the elongated structures and reduced magnitude of vorticity. Past the location of where the adverse pressure gradient appears, on the middle of the suction side, an unstable wavy thick boundary layer edge is formed with the recirculation bubble underneath. It is observed that where the FST is weak little turbulent momentum transport to the boundary layer takes place, thus allowing the distinctive large K-H instability structures to develop downstream. In case (Fig.19 (b)) the same phenomenon takes place, but the boundary layer is thinner. The wavy boundary layer edge and the K-H instability structures still exist. Note that as shown in [2], using the base mesh, the time-averaged shear stress profile shows a small negative region, indicating that the recirculation bubble still occasionally exists underneath the unstable boundary layer. Finally, using the finer mesh coupled with the high order scheme (Fig.19 (c)), the characteristic of the boundary layer instability and its transition to turbulence appears to significantly differ from the other two cases. The FST persists in the passage and interacts with the boundary layer. This effect and the increased TKE

content of the boundary layer (shown later) significantly suppresses the boundary layer growth and as a result the boundary layer thickness is much reduced. The K-H instability does not appear, the separation bubble vanishes, and the bypass mode of transition replaces bubble reattachment mechanism.

Based on the spectral analysis and the sensitivity analysis that we performed, we learned that the frequency of the hiccup is strongly connected to the predicted separation and reattachment activity on the suction side. Also, as shown in Fig. 19, the mechanism of the boundary layer instability seems to gradually change from separation, shear layer with K-H instability (very frequent hiccups) to bypass transition (no hiccup). This is consistent with the fact that the frequency of occurrence of the hiccups decreases and the phenomenon finally vanishes with using the denser grid or a higher order scheme.

b. Bounday Layer Profiles

For a better understanding of the momentum transfer and production of turbulence inside the boundary layer for H-FST4 (red), H-FST6 (green) and H-FST7 (blue), normalized axial velocity profiles inside the boundary layer at X/C_x=0.6, 6.5, 7, 7.5, 8, and 8.5 are plotted in Fig. 20. It is shown that the velocity profile appears "fuller" when using the denser grid (blue), which may then withstand adverse pressure gradient and therefore separation. The boundary layer is energized by the free stream turbulence via momentum transfer and also production of TKE within the boundary layer which together serve to prevent the flow from separating. The coarser grid, (green profile) shows early inflection in the boundary layer, near the wall (Fig.20 (a)), a sign of imminent separation**,** and experiences separation and is subsequently reattached at X/C_x =0.75, Fig. 20(d).

c. Turbulence Content

Figure 21 illustrates the effect of free stream turbulence by showing the TKE content normalized by the value of H-FST7 at corresponding probe locations inside the boundary layer. It is confirmed that the turbulence content inside the boundary layer at all probe locations $X/C_x \leq 0.7$ for H-FST7 is larger than for H-FST4 and H-FST6. In fact, approximately 60% of the TKE has been resolved for H-FST6 and even less for H-FST4 case. The higher TKE content of H-FST7 gives the resulting profile its ability to withstand separation consistent with our earlier conclusions.

CONCLUSIONS

LES simulations with different numerical settings, different free stream turbulence intensities, and different grid resolutions have been carried out to simulate the Variable Speed Power Turbine at low Reynolds numbers (Re_{ex} = 220,000). The predicted total pressure loss coefficients were compared to the experimental measurements acquired at the NASA Transonic Turbine Blade Cascade Facility (CW-22). The summary of all the predictions is provided in Table 4. The primary findings are listed as follows:

1. When a coarser mesh or a lower-order scheme is used, boundary layer separation is more likely to occur due to lack of turbulence production in the boundary layer which tends to be less resolved. Also, the momentum transport from the free stream turbulence tends to be underestimated. Both outcomes have a negative effect on the stability of the wake and the accuracy of the results.
2. Using the fine mesh and the high-order scheme, the prediction accuracy of the wake of the high-FST case is as successful as the low-FST case in terms of three metrics: the horizontal shift, the discrepancy in the maximum pressure loss coefficient, and the discrepancy in the full width at half height maximum.
3. Utilizing spectral analysis, it is possible to investigate the existence of valid correlational relationship between the wake flow and other effects, such as, the relationship to free stream turbulence buffeting on the leading edge and on the pressure side, as well as unsteady boundary layer separation and reattachment on the suction side.
4. A change in physics upon grid refinement should not take place as a condition of grid convergence. If there exists a boundary layer separation, a refinement in the grid should result in a similar dynamic behavior of the wake.

This study highlights the importance of the mesh requirements for LES simulations of the LPT wake. In the absence of experimental data, which is the primary reason for simulations, in addition to running the usual checks for LES simulations, spectral analysis may help to diagnose underlying issues with the simulations. In the present case, where flow separation is at issue, while time-averaged shear stress on the blade surface did not indicate flow separation, spectral analysis was able to provide information about its presence and its effect.

ACKNOWLEDGEMENTS

This work was supported by the Compact Gas Turbine sub-project managed by Ms. Kimlan Pham for the NASA Advanced Air Transport Technology project. Experimental data was provided by Dr. Paul Giel, which is appreciated. The authors also would like to thank Dr. David Rigby and Dr. Erlendur Steinthorsson for their assistance in preparing and running the simulations. The simulations were conducted on the NASA Advanced Supercomputing (NAS) Pleiades computer cluster.

NOMENCLATURE

AUSM	Advection Upstream Splitting Method
BC	Boundary Condition
CFD	Computational Fluid Dynamics
C_x	axial chord
DNS	Direct Numerical Simulation
FFT	Fast Fourier Transform
FST	Freestream Turbulence
FWHM	Full Width at Half Maximum
h	span
h_δ	spanwise boundary layer thickness
$L_{s,0}, L_{s,1}$	axial location of upstream and downstream measurement stations 0 and 1
LDKM	Localized Dynamic Kinetic Model
LES	Large-Eddy simulation
LPT	Low-pressure Turbine
K-H	Kelvin-Helmholtz
Ma	Mach number
r	correlation coefficient
RANS	Reynolds-Averaged Naiver-Stokes
Re	Reynolds number

TKE	turbulence kinetic energy
Ts	turbulent length scale
Tu	turbulence intensity
u, v, w	velocity component
VSPT	Variable Speed Power Turbine
X, Y, Z	Cartesian coordinate
β	Inflow flow angle
$\mathcal{M}$	Pope criterion
ΔX	horizontal shift at the peak
ΔC_{pt}	discrepancy in maximum pressure loss coefficient
ΔW	difference between the FWHMs of the data and the prediction

SUBSCRIPTS

0	upstream location
1	downstream location
in	Based on inlet conditions
ex	Based on exit conditions
rms	root mean square
X	Axial

REFERENCES

[1] Marconcini, M., Pacciani, R., Arnone, A., Michelassi, V., Pichler, R., Zhao., Y., & Sandberg, R., 2018, "Large Eddy Simulation and RANS Analysis of the End-Wall Flow in a Linear Low-Pressure-Turbine Cascade: Part II: Loss Generation." Journal of Turbomachinery: 141 (5), 051004.

[2] Miki, K., Ameri, A., 2020, “Large-Eddy Simulation of The Variable Speed Power Turbine Cascade with Inflow Turbulence”, Proceedings of the ASME Turbo Expo, Virtual, September 2020, GT2020-14140.

[3] Ameri, A., 2016, “Requirements for LES Computations of VSPT Flows”, NASA CR-2016-218962.

[4] Przytarski, PJ, & Wheeler, APS. 2018, “Accurate Prediction of Loss Using High Fidelity Methods", Proceedings of the ASME Turbo Expo, Oslo, Norway, June 2018, GT2018-77125.

[5] Pichler, R., Sandberg, R. D., Michelassi, V., 2016, “Assessment of Grid Resolution Requirements for Accurate Simulation of Disparate Scales of Turbulent Flow in Low-Pressure Turbines”, Proceedings of the ASME Turbo Expo, Seoul, South Korea, June, 2016, GT2016-56858.

[6] Lee, Y., Teramoto, S., Toki, T., Okamoto, K., 2020, “Effect of the large Eddy Simulation Calculation Parameters on Prediction of Profile Loss in an Axial Cascade at Off-Design Incidence”, Proceedings of the ASME Turbo Expo, Virtual, 0September, GT2020-14554.

[7] Medic, G., Zhang, V., Wang, G., Joo, J., and Sharma, O. P., 2016, “Prediction of Transition and Losses in Compressor Cascades Using Large-Eddy Simulation”, Journal of Turbomachinery: 138(12), 151001.

[8] Harnieh, M., Gicquel, L., Duchaine, F.. "Large Eddy Simulations of a Highly Loaded Transonic Blade with Separated Flow." Proceedings of the ASME Turbo Expo, Oslo, Norway, June 2018, GT2018-75730.

[9] Ameri, A., 2018, “Implicit-LES simulation of variable-Speed Power Turbine Cascade for Low Free-Stream Turbulence Conditions”, Proceedings of the ASME Turbo Expo, Oslo, Norway, June 2018, GT2018-77120.

[10] Comte-Bellot, G., Corrsin, S., 1971, “Simple Eulerian Time Correlation of Full-and Narrow-band Velocity Signals in Grid-generated, Isotropic Turbulence”, Journal of Fluid Mechanics:48, 273-337.

[11] Pope, S., 2004, “Ten Questions Concerning the Large-Eddy Simulation of Turbulent Flows”, New Journal of Physics: 6, 32.

[12] Sandberg, R.D., Pichler, R., Chen, L., 2012, “Assessing the sensitivity of turbine cascade flow to inflow disturbances using direct numerical simulation”, Proceedings of the 13th International Symposium for Unsteady Aerodynamics, Aeroacoustics and Aeroelasticity in Turbomachinery (ISUAAAT), Japan. 11 - 14 Sep 2012.

[13] McVetta, A. B., Giel, P. W., Welch. G. E., 2013, “Aerodynamic Measurements of a Variable-Speed Power-Turbine Blade Section in a Transonic Turbine Cascade at Low Inlet Turbulence", Proceedings of the ASME Turbo Expo, San Antonio, Texas, June 2013, GT2013-94695.

[14] Flegel, A.B., Giel, P.W., Welch, G. E., 2014, “Aerodynamic Effects of High Turbulence Intensity on a Variable-Speed Power-Turbine Blade with Large Incidence and Reynolds Number Variations”, Proceedings of the 50th Joint Propulsion Conference and Exhibit, AIAA Paper 2014-3933.

[15] Thurman, D., Flegel, A., Giel, Pau., 2014, “Inlet Turbulence and Length Scale measurements in a Large-Scale Transonic Turbine Cascade”, Proceedings of the 50th AIAA Joint Propulsion Conference, AIAA 2014-3934.

[16] Giel, P., Shyam, V., Juangphanich, P., Clark, J. P., 2020, “Effects of Trailing Edge Thickness and Blade Loading Distance on the Aerodynamic Performance of Simulated CMC Turbine Blades”, Proceedings of the ASME Turbo Expo, Virtual, September 2020, GT2020-15802.

[17] Steinthorsson, E., Liou. M-S. Povinelli, L., 1993, “Development of an Explicit Multiblock/Multigrid Flow Solver for Viscous Flows in Complex Geometries," Proceedings of the 29th Joint Propulsion Conference and Exhibit, AIAA Paper 1993-2380.

[18] Liou, M.-S., 2006, “A Sequel to AUSM, Part II: AUSM+-up for All Speeds", Journal of Computational Physics: 214, 137-170.

[19] Cada, M., Torrilhon, M., 2009, “Compact third-order Limiter Functions for Finite Volume Methods”, Journal of Computational Physics: 228, 4118-4145.

[20] Kim, W.-W. Menon, S., 1995, “A New Dynamic One-equation Subgrid-scale Model for Large Eddy Simulations," Proceedings of the 33rd AIAA Aerospace Sciences Meeting and Exhibit, January 1995, AIAA Paper 1995-356.

[21] Lilly, D. K., 1992, “A Proposed Modification of the Germano Subgrid-scale Closure Method", Physics of Fluids: 4, 633-635.

[22] Cui, J., Rao, V. N., Tucker, P., 2016, “Numerical Investigation of Contrasting Flow Physics in Different Zones of a High-Lift Low-Pressure Turbine Blade”, Journal of Turbomachinery*:* 138*,* 011003.

[23] Klein, M., Sadiki, A., Janicka, J., 2003, “A Digital Filter Based Generation of Inflow Data for Spatially Developing Direct Numerical or Large Eddy Simulations", Journal of Computational Physics: 186, 652-665.

[24] Simon, T. W., Qiu, S., Yuan, K., 2000, ‘‘Measurements in a Transitional Boundary Layer Under Low-Pressure Turbine Conditions’’, NASA/CR-2000-209957.

[25] Volino, R., 2002, “Separated Flow Transition Under Simulated Low-Pressure Turbine Airfoil Conditions—Part 2: Mean Flow and Turbulence Statistics”, Journal of Turbomachinery: 124, 656-663.

TABLE

TABLE 1: GEOMETRY PARAMETERS OF VSPT BLADE

Geometry	Value
Chord, C_x	180.57 [mm]
True Chord	194.44 [mm]
Pitch	130.00 [mm]
Span, h	152.40 [mm]
Axial location of St., 0, $L_{S,0}/C_x$	-0.415
Axial location of St., 1, $L_{S,1}/C_x$	1.07
Leading Edge Diameter	15.16 [mm]
Trailing Edge Diameter	3.30 [mm]

TABLE 2: TEST CONDITIONS

	Low-FST	High-FST
Press. Ratio	1.0891	1.0862
Re_{ex}	220,000	220,000
Ma_{in}/Ma_{ex}	0.263/0.351	0.249/0.346
Tu [%]	0.5	10, 15
Ts/C_x	0.02	0.07
h_δ/S	0.25	0.1
β [deg]	40	40

TABLE 3: CHARACTERLISTIC OF PREDICTED INCOMING TURBULENCE AND EXPERIMENTAL DATA [15]

LES (H-FST1)						Exp. reference [15]		
X/C_x= -1	X/C_x= -0.5					X/C_x = -0.415		
Tu [%]	Tu [%]	$u'_{rms}/\overline{U}_0$	$v'_{rms}/\overline{U}_0$	$w'_{rms}/\overline{U}_0$	$(u'v')^{1/2}/\overline{U}_0$, $(u'w')^{1/2}/\overline{U}_0$, $(v'w')^{1/2}/\overline{U}_0$	Tu [%]	Spanwise variance ($\pm\Delta Tu$)	Pitch variance ($\pm\Delta Tu$)
15.6	13.2	0.072	0.083	0.074	< 0.001	9.4%	4.1%	15%

TABLE 4: SUMMARY OF WAKE PREDICTION

	Numerical Setting					Results			
	Tu [%]	*Ts*	Mesh size [Million]	Order	Stable wake?	*Tu* [%] At *X/Cx*=- 0.5	ΔX	ΔC_{P_t}	$\lvert\Delta W_{exp}-\Delta W_{LES}\rvert/\Delta W_{exp}$ (FWHM) [%]
L-FST	0.05	0.07	85	2	-	-	0.05	0.03	0.38
H-FST 1	15	0.07	85	2	No	13.2	0.10	0.15	67.4
H-FST 2	15	0.07	10	2	No	11.6	0.12	0.20	102.9
H-FST 3	10	0.07	10	2	No	8.0	0.13	0.23	82.9
H-FST 4	10	0.07	10	3	No	8.1	0.11	0.15	74.8
H-FST 5	15	0.07	85	3	Yes	14.1	0.08	0.09	53.6
H-FST 6	10	0.07	85	3	Yes	9.2	0.11	0.13	53.6
H-FST 7	10	0.07	170	3	Yes	9.7	0.06	0.04	4.4

FIGURE

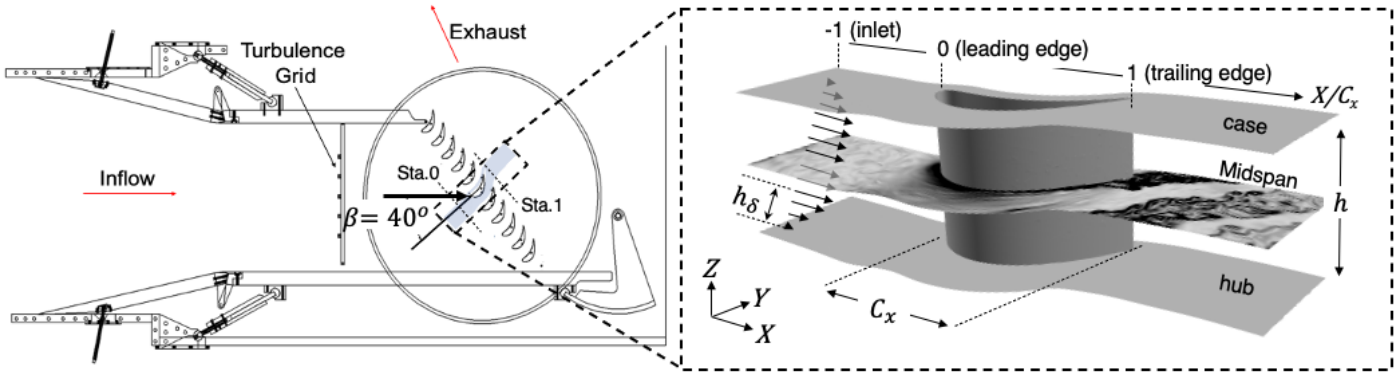

(a) Experimental setup (top view) (b) Computational setup (suction side)

FIGURE 1: OVERVIEW OF EXPERIMENTAL AND NUMERICAL CONFIGURATIONS.

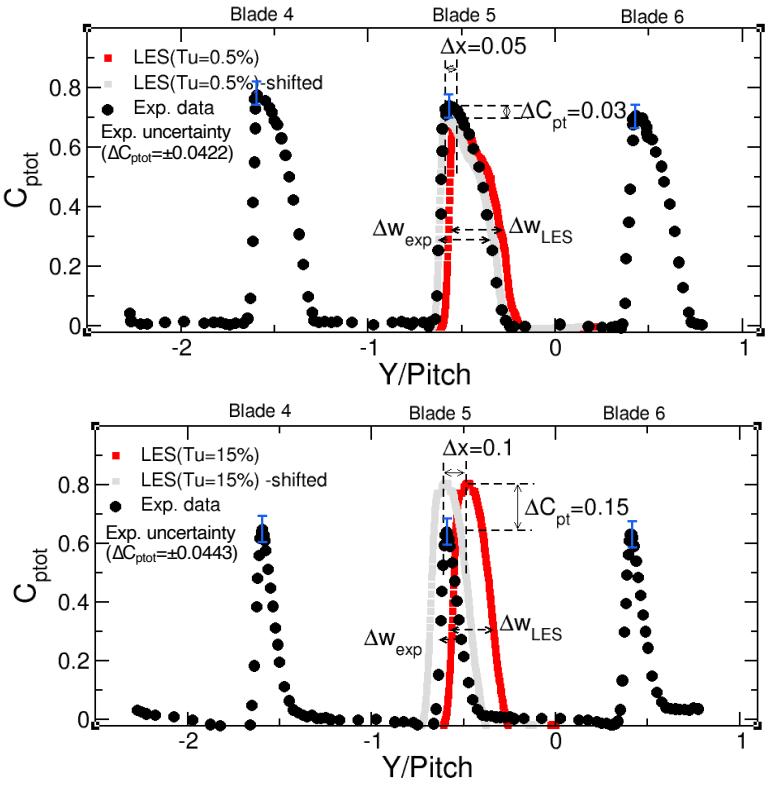

FIGURE 2: TOTAL PRESSURE LOSS COEFFICENT IN THE WAKE (X/C_x=1.07) FOR (a) THE LOW-FST CASE AND (b) THE HIGH-FST CASE (TU=15%)

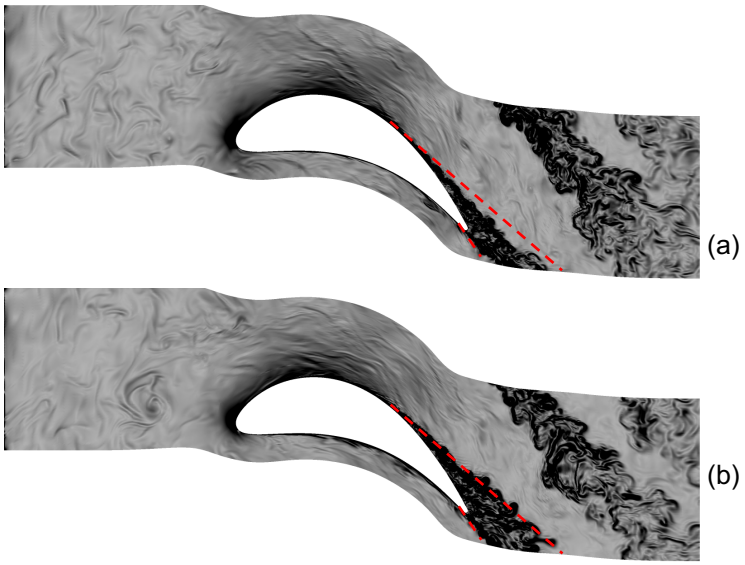

FIGURE 3: GRADIENT OF DENSITY AT THE MIDSPAN (Z/h=0.5) FOR (a) STABLE INSTANCE AND (b) UNSTABLE INSTANCE OF THE HIGH-FST CASE (TU=15%)

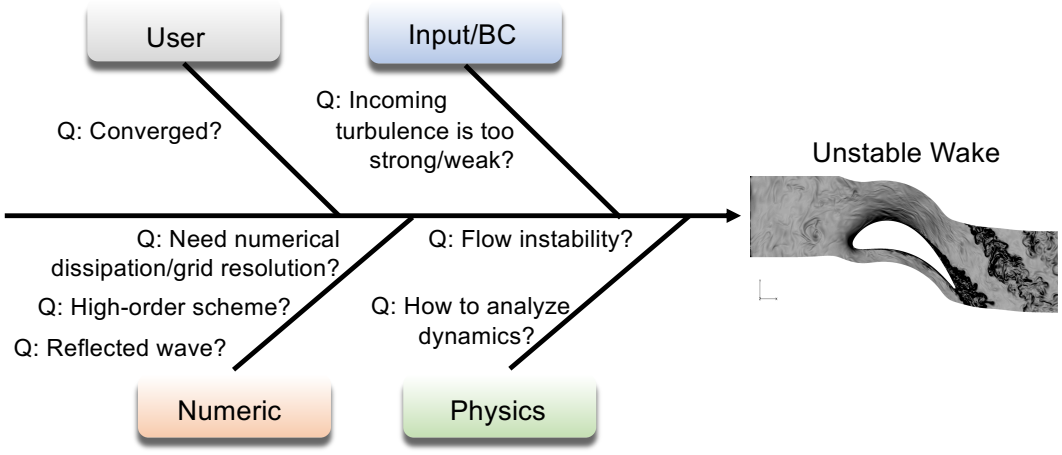

FIGURE 4: FISHBONE DIAGRAM OF UNSTABLE WAKE ANALYSIS

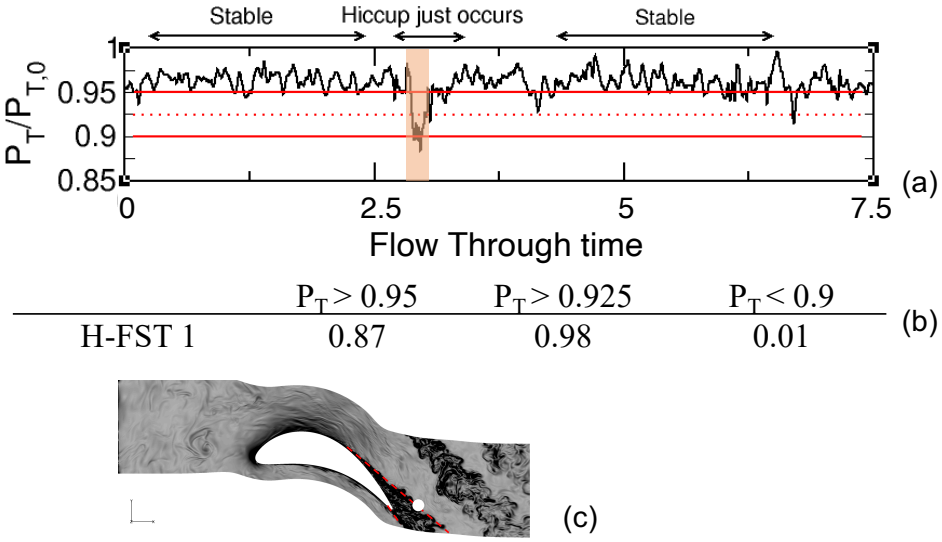

FIGURE 5: (a) TIME-HISTORY OF TOTAL PRESSURE AT THE WAKE AND (b) STATISTICS OF NORMALIZED TIME INTERVAL AND (c) PROBE LOCATION (WHITE CIRCLE)

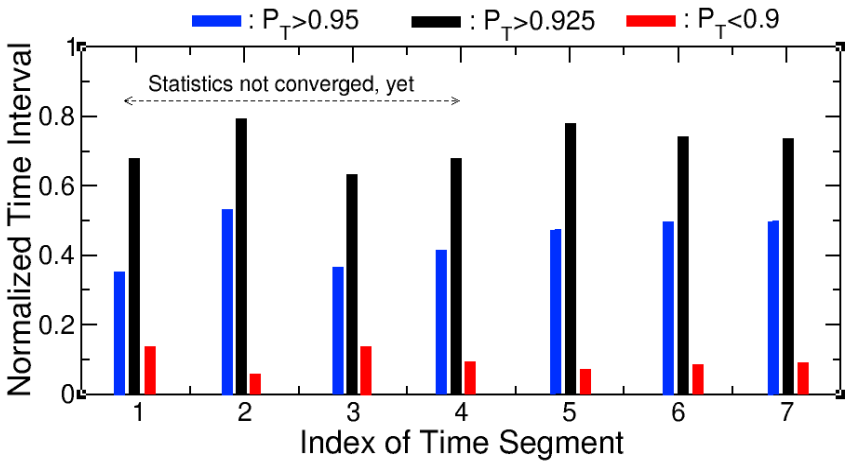

FIGURE 6: NORMALIZED TIME INTERVALS OF SEVEN TIME SEGMENTS FOR H-FST 2 (10M MESH, TU=15%)

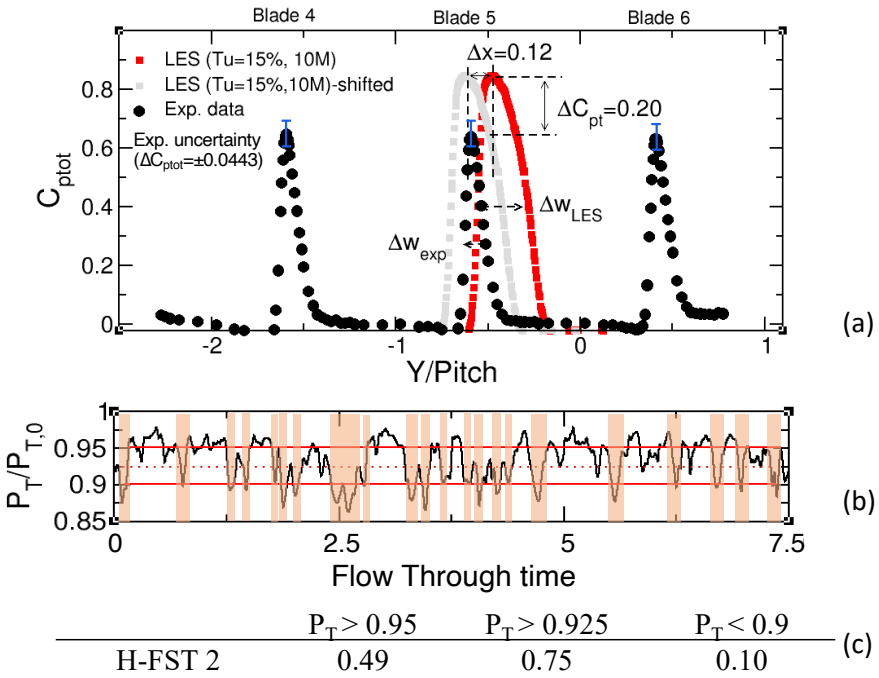

FIGURE 7: (a) TOTAL PRESSURE LOSS COEFFICENT IN THE WAKE (X/C_X=1.07), (b) TIME-HISTORY OF TOTAL PRESSURE AT THE WAKE, AND (c) STATISTICS OF NORMALIZED TIME INTERVAL FOR H-FST 2 (10M MESH, TU=15%)

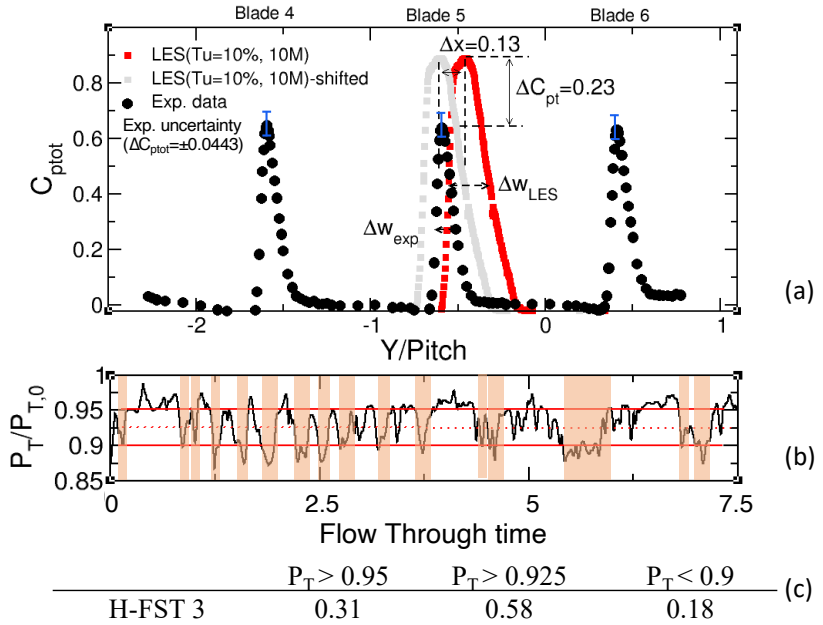

FIGURE 8: (a) TOTAL PRESSURE LOSS COEFFICENT IN THE WAKE (X/C_X=1.07), (b) TIME-HISTORY OF TOTAL PRESSURE AT THE WAKE, AND (c) STATISTICS OF NORMALIZED TIME INTERVAL FOR H-FST 3 (10M MESH, *TU*=10 %)

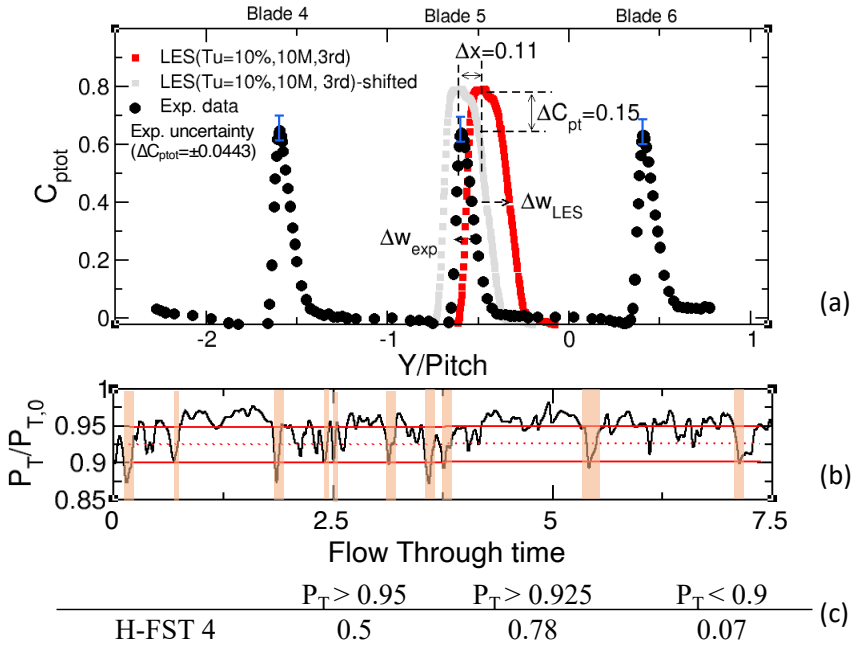

FIGURE 9: (a) TOTAL PRESSURE LOSS COEFFICENT IN THE WAKE (X/C_X=1.07), (b) TIME-HISTORY OF TOTAL PRESSURE AT THE WAKE, AND (c) STATISTICS OF NORMALIZED TIME INTERVAL FOR H-FST 4 (10M MESH, *TU*=10 %, HIGH-ORDER SCHEME)

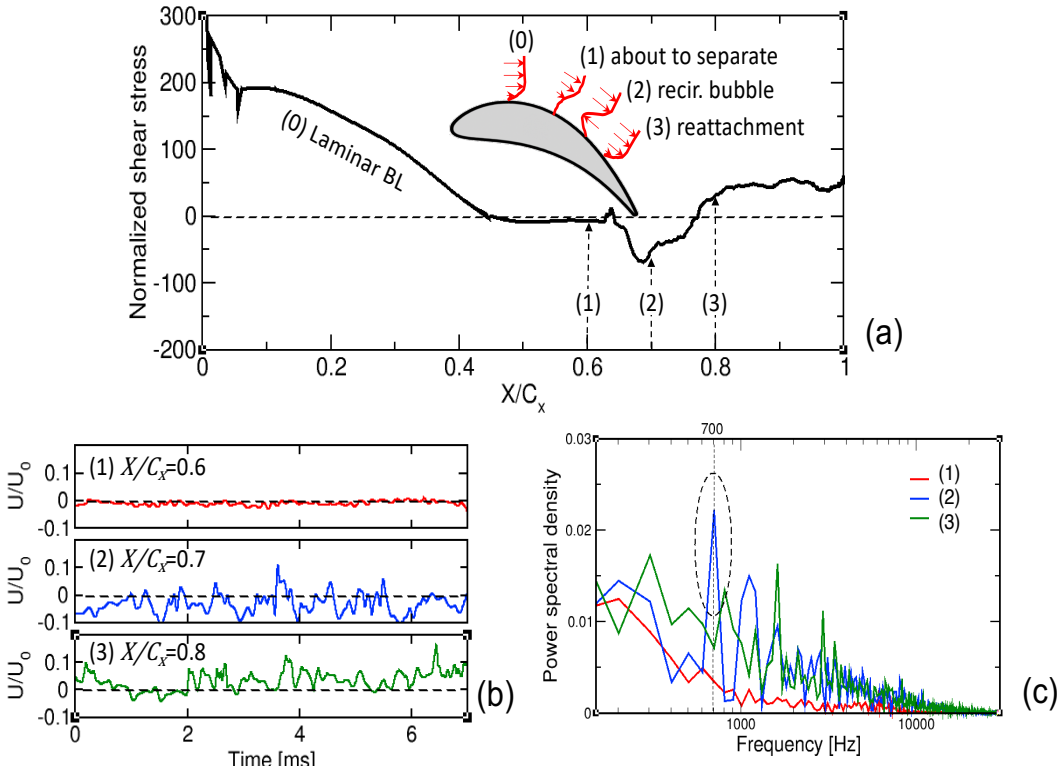

FIGURE 10: (a) TIME-AVERAGED SHEAR STRESS AT THE MIDSPAN, (b) TIME-HISTORIES OF AXIAL VELOCITY AND (c) FFT OF AXIAL VELOCITY AT THREE DIFFERENT LOCATIONS NEAR THE SEPARATION POINTS [2]

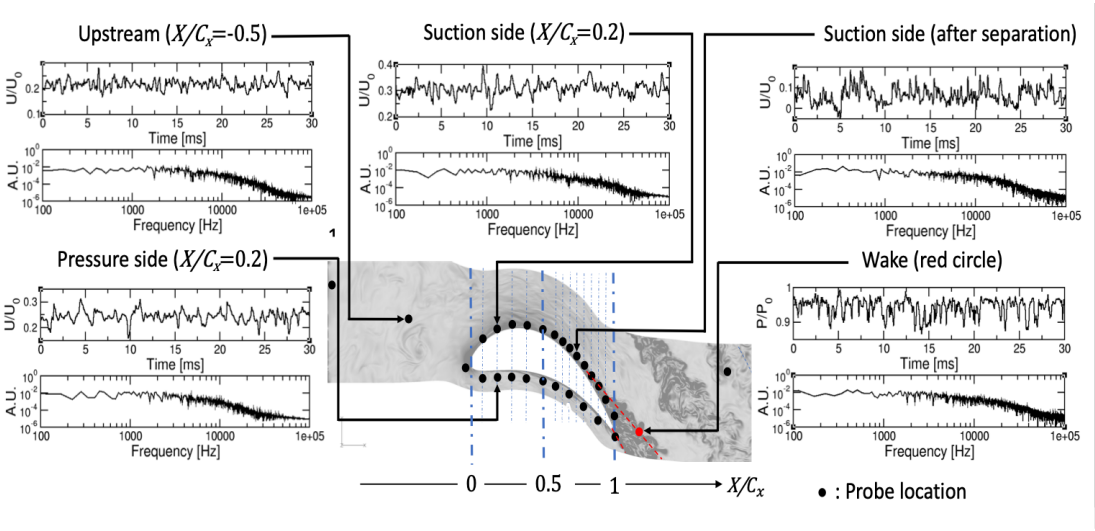

FIGURE 11: TIME-HISTORIES OF NORMALIZED AXIAL VELOCITY AND POWER SPECTRAL DENSITITES FOR H-FST 3

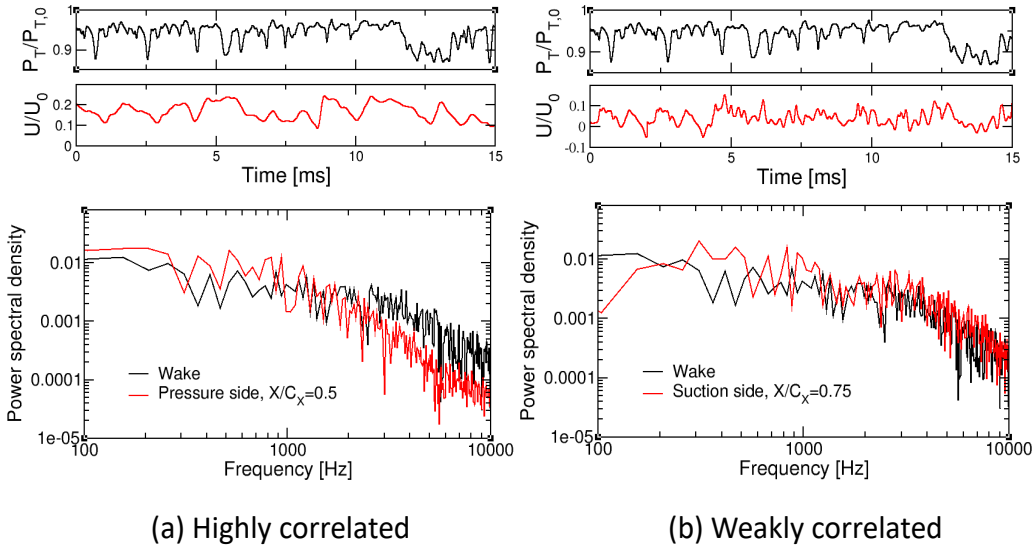

FIGURE 12: TIME-HISTORIES OF NORMALIZED AXIAL VELOCITY COMPONENTS AND POWER SPECTRAL DENSITITES FOR (a) CORRELATION COEFF. = 0.71 AND (b) CORRELATION COEFF. = 0.33 FOR H-FST4.

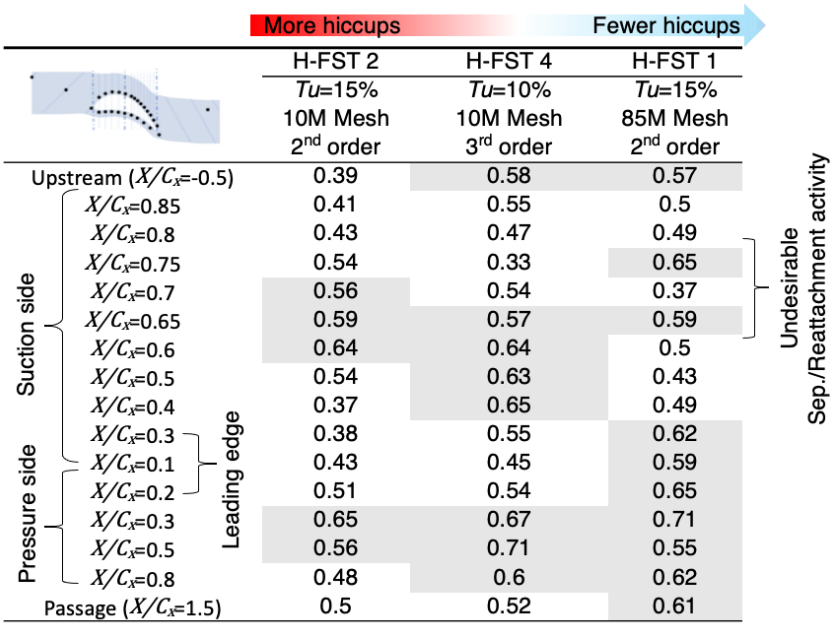

FIGURE 13: CORRELATION COEFFICENTS OF SELECTED TEST CASES (H-FST1, H-FST2, AND H-FST4). THE SHADING (GRAY) INDICATES RELATIVELY HIGH CORRELATIONS

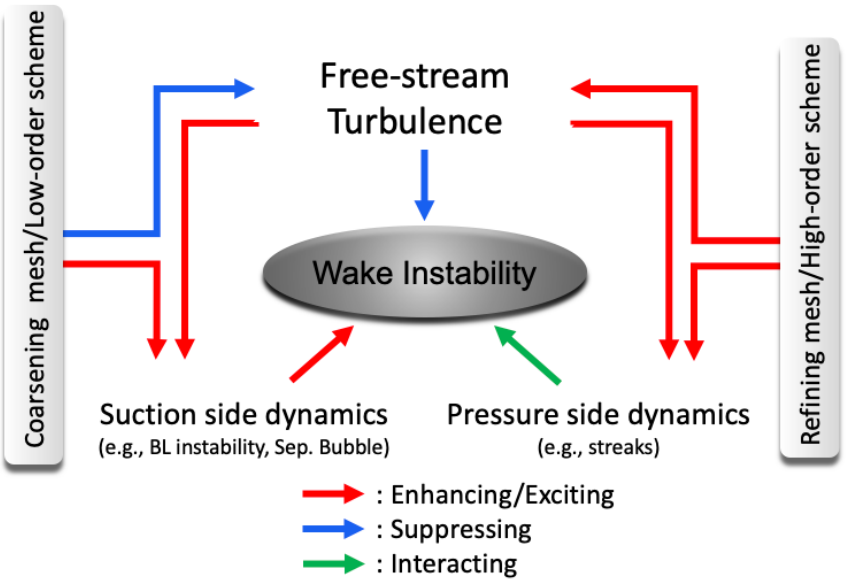

FIGURE 14: CHART OF THE UNSTABLE WAKE MECHANISM

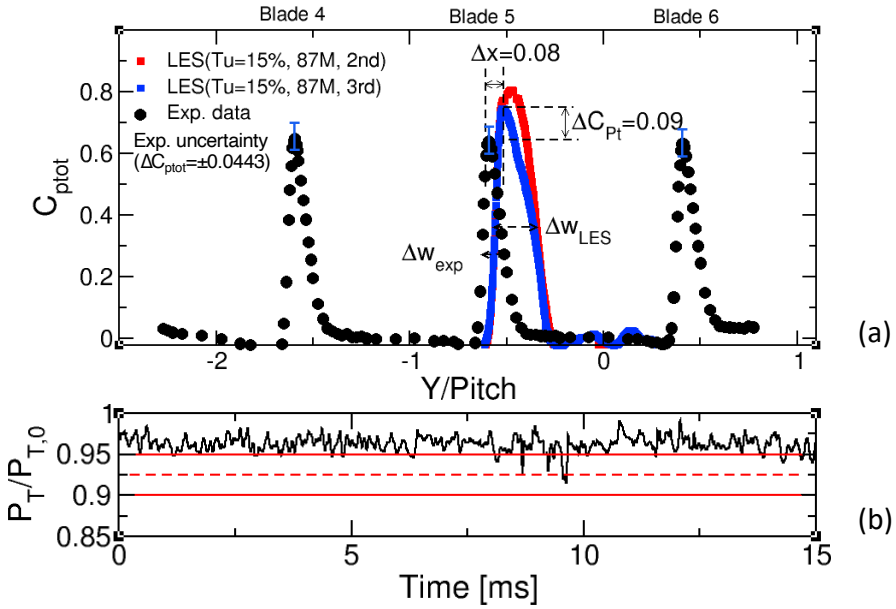

FIGURE 15: (a) TOTAL PRESSURE LOSS COEFFICENT IN THE WAKE (X/C_X=1.07) FOR H-FST 1 (RED) AND H-FST 5 (BLUE) AND (b) TIME-HISTORY OF TOTAL PRESSURE AT THE WAKE (H-FST5)

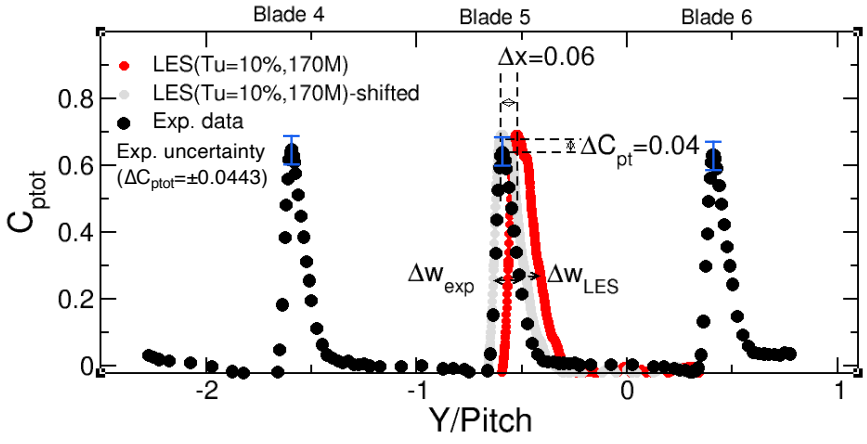

FIGURE 16: TOTAL PRESSURE LOSS COEFFICENT IN THE WAKE (X/C_X=1.07) USING THE FINE MESH (H-FST 7)

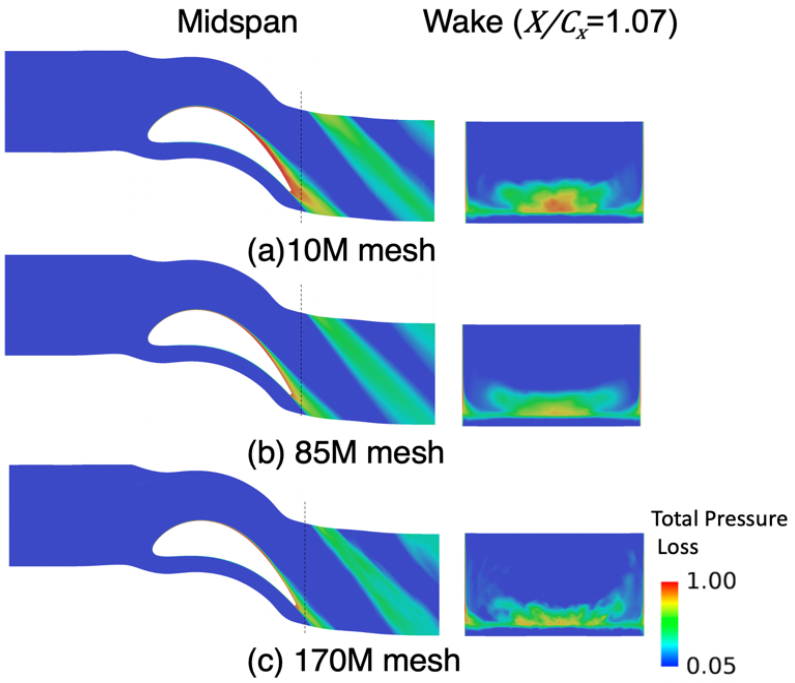

FIGURE 17: TOTAL PRESSURE

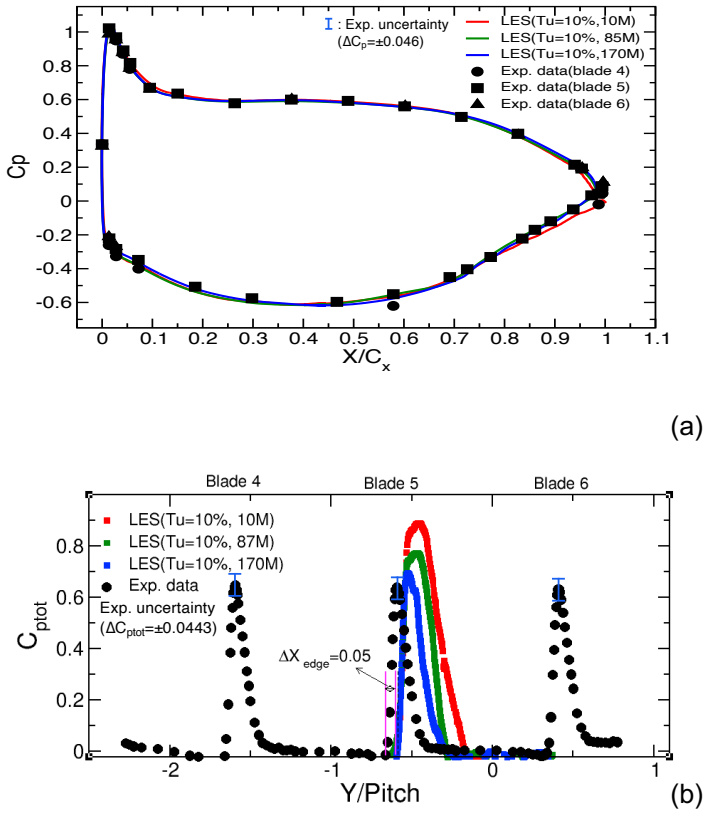

FIGURE 18: (a) PRESSURE LOADING ON THE BLADE AT THE MIDSPAN AND (b) TOTAL PRESSURE LOSS COEFFICENT IN THE WAKE (X/C_x=1.07) USING A THIRD-ORDER SCHEME AND TU=10%. 10 MILLION GRID (RED), 85 MILLION GRID (GREEN) AND 170 MILLION GRID (BLUE).

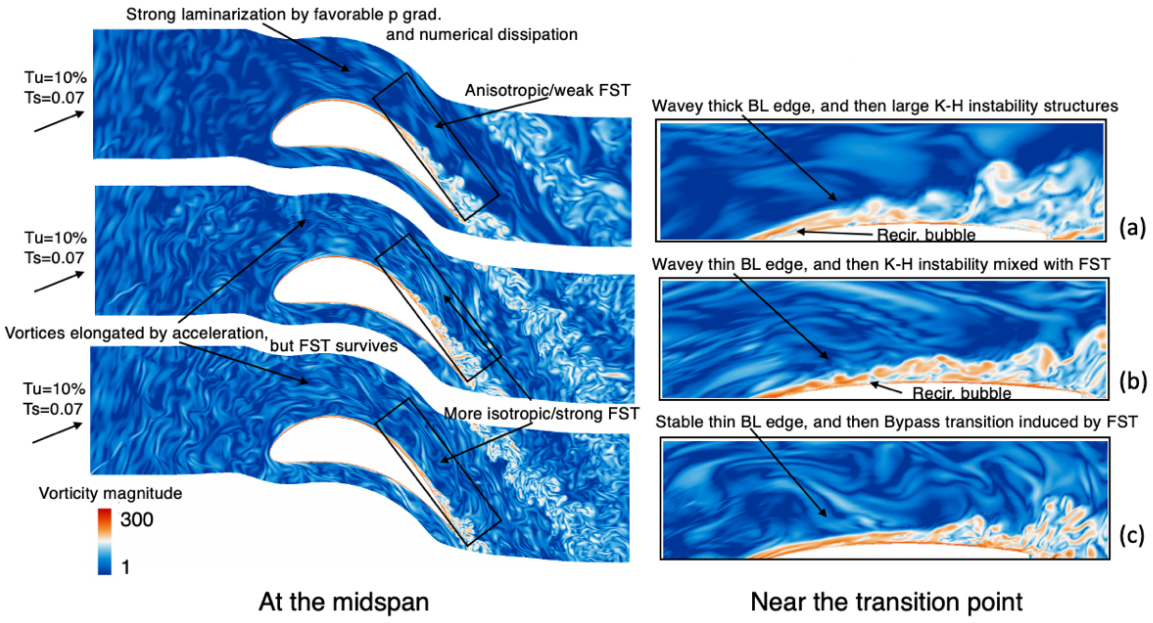

FIGURE 19: INSTANTENEOUS VORTICITY MAGNITUDE AT THE MID-SPAN OF (a) H-FST4, (b) H-FST6 ANS (c) H-FST7

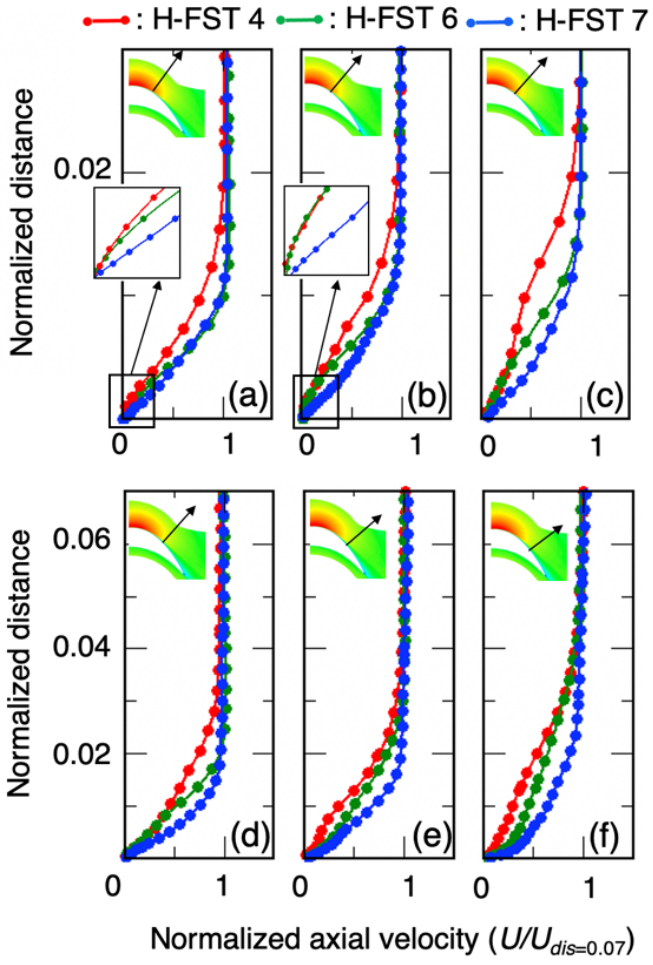

FIGURE 20: TIME-AVERAGED AXIAL VELOCITY PROFILES NEAR SEPERATION POINT OF H-FST4, H-FST6 AND H-FST7 AT (a) X/C_x=0.6, (b) X/C_x=0.65, (c) X/C_x=0.7, (d) X/C_x=0.75, (e) X/C_x=0.8, AND (f) X/C_x=0.85

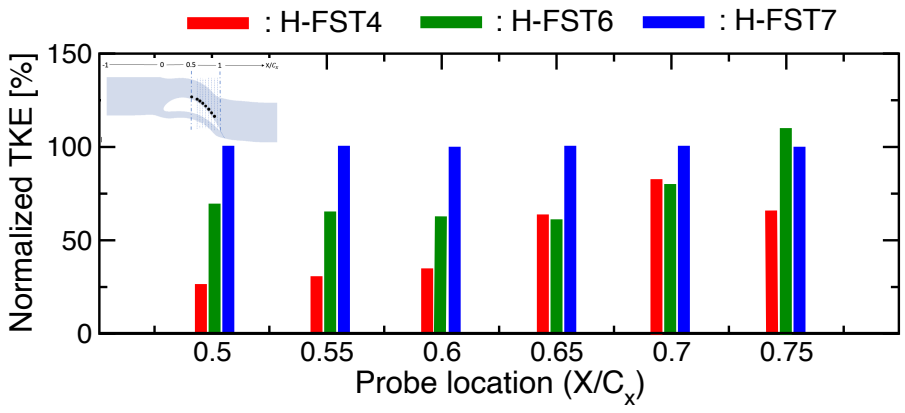

FIGURE 21: TIME-AVERAGED NORMALIZED TURBULENCE KINETIC ENERGY INSIDE THE BOUNDAY LAYER